AIAA JOURNAL
Vol. 50, No. 10, October 2012

Large-Eddy Simulation of Shock/Cooling-Film Interaction

Martin Konopka,* Matthias Meinke,† and Wolfgang Schröder‡
RWTH Aachen University, 52062 Aachen, Germany

DOI: 10.2514/1.J051405

The interaction of shock waves with supersonic cooling films is analyzed using large-eddy simulations. The laminar cooling flow is injected at Mach 1.2 through a slot into a fully turbulent boundary layer at Mach 2.44. For this injection condition, three configurations are investigated. A zero-pressure-gradient flow is compared with two configurations where shock waves are generated by a flow deflection of 5 deg. The shock waves impinge onto the cooling flow at two positions downstream of the slot. When the impingement is located within the potential-core region of the cooling flow, the adiabatic cooling effectiveness is reduced by as much as 36% compared to the zero-pressure-gradient configuration because the shock/cooling-film interaction excites a transition of the laminar slot boundary layer. Additionally, turbulence levels are significantly increased by the shock wave, and high temperature fluctuations occur. When the shock-wave impingement is located further downstream of the slot, there is an even steeper slope in cooling effectiveness in the streamwise direction. That is, the slope is 37 and 21% steeper compared to the zero-pressure gradient and the potential-core cases. The turbulent Prandtl number varied over the flow region of the shock/cooling-film interaction from 0.5 to 2.

Nomenclature

c_f	=	skin-friction coefficient
c_p	=	heat capacity at constant pressure
f	=	convective heat transport term
k	=	turbulent kinetic energy
L	=	domain length
M	=	blowing rate
Ma	=	Mach number
m	=	cooling effectiveness gradient
Pr	=	Prandtl number
p	=	pressure
r	=	length of the potential-core region
S	=	slot height
T	=	temperature
t	=	time
u, v, w	=	streamwise, wall-normal, and spanwise velocity components
β	=	flow deflection angle
δ	=	boundary-layer thickness
η	=	cooling effectiveness
Θ	=	dimensionless fluid temperature
μ	=	dynamic viscosity
ν	=	kinematic viscosity
ρ	=	density

Subscripts

aw	=	adiabatic wall
e	=	boundary-layer edge
i	=	Cartesian component
i	=	injection condition at the slot
imp	=	shock-impingement position
pt	=	pitot pressure
pt∞	=	freestream pitot pressure
r∞	=	freestream recovery temperature
ri	=	cooling flow recovery temperature
sep	=	separation
t	=	total, turbulent
t∞	=	freestream total temperature
ti	=	cooling flow total temperature
VD	=	van Driest transformation
v	=	wall-normal heat transport
w	=	wall
τ	=	friction velocity
3	=	condition downstream of the reflected shock
∞	=	freestream conditions

Superscripts

$+$	=	inner wall units
$-$	=	Reynolds average
$'$	=	Reynolds fluctuation
$\sim$	=	Favre average
$''$	=	Favre fluctuation
$*$	=	coordinate originating at the wall

Received 7 June 2011; revision received 28 February 2012; accepted for publication 29 February 2012.

*Research Associate, Institute of Aerodynamics, Wüllnerstrasse 5a. Student Member AIAA.
†Senior Scientist, Institute of Aerodynamics, Wüllnerstrasse 5a.
‡Professor, Institute of Aerodynamics, Wüllnerstrasse 5a. Member AIAA.

I. Introduction

SUPERSONIC combustion ramjet (scramjet) powered vehicles flying at supersonic or hypersonic Mach numbers undergo an intense aerodynamic heating on the vehicle's outer surfaces and in the engine's interior such as the isolator, combustion chamber, and nozzle walls [1]. Because no radiation cooling for the internal flow of the scramjet is possible, active thermal protection is required. Supersonic film cooling is a promising concept to achieve engine surface temperature reduction, which was demonstrated first by experiments in turbulent and laminar flow [2–4]. In these studies, the cooling flow was injected through a slot. In a scramjet, the supersonic film cooling flow is affected by shock waves in the isolator and in the combustion chamber. In the literature, two classes of shock/cooling-interaction studies exist. In the first class, the impact of shock waves on the heat transfer rate is investigated. In the second class, the impact of shock waves on the adiabatic cooling effectiveness is studied. It is important to distinguish between these two classes because shock interaction could change the heat transfer into the wall by affecting the heat transfer coefficient without changing adiabatic effectiveness. Therefore, studies considering the heat transfer are discussed first, followed by studies considering adiabatic cooling effectiveness.

The interaction of shock waves with a supersonic film injected into a turbulent boundary layer was first studied experimentally in great

detail by Alzner and Zakkay [5]. An axisymmetric wedge around an axisymmetric centerbody was used to investigate the effects of injection on heat transfer and separation characteristics of incipient shock waves. They found injection to reduce the peak heat transfer at the shock-impingement location. However, the shock-impingement location was not specified at all considered cases, i.e., the state of the wall-bounded flow upstream of the shock/cooling-film interaction was not given. In Fig. 1, the three flow regions of turbulent film cooling with laminar slot injection are depicted [6,7] for the injection of a fluid with an injection velocity lower than the freestream velocity. Velocity profiles can be used to identify, e.g., the length of the potential-core region, for a coolant with a high molecular weight like air because the injection velocity is much lower than the freestream velocity. In the potential-core region right downstream of the slot, the flow is laminar and is encompassed by the upper shear layer and the laminar slot boundary layer at the wall. Further downstream, the mixing layer, which emanates from the lip, merges with the laminar slot boundary layer. This region is the wall-jet region, where intense mixing takes place. It then forms the boundary-layer region, where the cooling stream and the freestream still mix, but the time-averaged velocity profiles already possess the shape like an undisturbed fully turbulent boundary layer. Considering the streamwise variation of the wall-bounded flow and the significance of the state of the upstream near-wall flow for the fundamental shock/boundary-layer interaction problem, it is necessary to analyze the film cooling efficiency in supersonic choked flow depending on the structure of the near-wall flow or, in other words, on the location of the shock impingement upon the cooling film. The following survey on the literature will show that some contradictory results exist that are related to the aforementioned issue of the state of the boundary layer upstream of the shock impingement.

Kamath et al. [8] compared experimental heat flux data with computational results based on the Reynolds-averaged Navier–Stokes (RANS) approach using the high Reynolds number version of the two-equation model of Coakley [9]. They found film cooling to reduce the peak heat flux due to the shock impingement. However, they did not specify the flow region at the shock-impingement location, and the parabolic code was not able to capture separation. Olsen et al. [10] found in their measurements no effect of the shock-impingement location on peak heat flux over the investigated cooling length, but they did not define any velocity profiles upstream of the shock impingement indicating the flow region. Holden et al. [11] compared their experimentally obtained heat transfer results with and without cooling with the findings from [5]. Unlike Alzner and Zakkay [5], they found that film cooling has little or no effect on the peak heat transfer. This discrepancy was explained by Juhany and Hunt [12], who concluded that Holden et al. [11] considered shock waves impinging onto the wall-bounded flow 60 to 90 slot heights downstream of the slot, whereas the results of Alzner and Zakkay [5] were obtained for film cooling injection directly into the separation bubble.

Next, studies investigating shock/cooling interactions at adiabatic walls are discussed. Juhany and Hunt [12] investigated shock/cooling-film interaction in the wall-jet or boundary-layer region (Fig. 1) but did not investigate a position within the potential-core region. They found the shock waves to have no large effect on the recovery temperature at the adiabatic wall as long as no separation occurs. A further experimental study was conducted by Kanda et al. [13,14], in which shock-impingement locations right behind and 90 slot heights downstream of the point of injection were investigated.

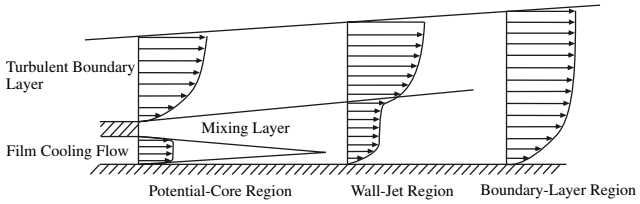

Fig. 1 Flow schematic with velocity profiles indicating the three distinct flow regions [6,40].

They found only a minimum effect on adiabatic cooling effectiveness and concluded that mixing between the cooling flow and the freestream was not significantly enhanced. This contradicts the previously mentioned results of Kamath et al. [8], who found the peak heat transfer at the wall to be increased by shock wave interaction. The difference could be caused by the different ramp lengths of the shock generators used. In the work of Kanda et al. [13], the shock wave of the leading edge of the shock generator interacted only 10 slot heights downstream of the shock-impingement point with an expansion wave created by the trailing edge of the shock generator. An expansion is known to damp turbulence and thus lowers the mixing of the cooling stream and freestream. Kamath et al. [8] used a much longer shock generator and the expansion wave impinged upon the cooling flow at 50 to 70 slot heights downstream of the shock wave. That is, downstream of the shock-interaction region different flowfields exist. Moreover, it has to be emphasized that the study of Kamath et al. [8] belongs to the heat transfer studies and the work of Kanda et al. [13,14] belongs to adiabatic effectiveness studies, which may not be directly compared. Takita and Masuya [15] performed RANS computations using the k–ε turbulence model and compared the adiabatic cooling effectiveness at the shock-impingement location with that of Kanda et al. [13], confirming the decrease of cooling effectiveness values to be only caused by the reduction of the local Mach number. On the other hand, Peng and Jiang [16] found in their RANS study based on the two-equation Menter shear stress transport [17] turbulence model considering the adiabatic cooling effectiveness that shock waves not only reduce the local Mach number but also enhance the mixing between the coolant and the freestream. Hyde et al. [18] experimentally studied a shock wave impinging onto the potential-core region. They measured significant total temperature fluctuations determining the mixing of the cooling flow with the freestream boundary layer.

As stated previously, the brief literature overview shows that in many of the previous studies, film-cooling effectiveness based on the heat transfer or adiabatic wall temperature was investigated without varying or without specifying the location of the shock-impingement point. In other studies, the shock/boundary-layer interaction was perturbed by additional outer effects like expansion waves such that no uniquely defined shock/cooling-film problem was analyzed. Therefore, in this numerical study, the adiabatic cooling effectiveness will be investigated at clearly defined flow conditions upstream of the impingement of the shock upon the cooling film. No downstream generated perturbations will impact the shock/cooling-film interaction. Two shock/cooling-film configurations will be discussed, which differ by the impingement location. In the first configuration the shock impinges upon the cooling film in the potential-core region, and in the second configuration the shock-impingement point is located further downstream in the boundary-layer region (Fig. 1). The results of these two cases where an adverse-pressure gradient due to an impinging shock occurs are also related to a zero-pressure-gradient case, i.e., a configuration without a shock wave impinging upon a cooling film.

The paper is organized as follows. First, the various film-cooling configurations are schematically described. Next, the numerical method is presented, followed by a description of the boundary conditions and the computational mesh. Subsequently, the geometry and the flow parameters defining the three flow problems are given. In the discussion of the results, first the generation of the turbulent inflow data is validated, and the numerical adiabatic cooling effectiveness and flow profiles are compared with experiments conducted by Juhany et al. [7] as well as Juhany and Hunt [12]. Then, the impact of shock waves on supersonic film cooling is discussed in terms of cooling effectiveness and turbulent transport of heat and momentum. Finally, some conclusions are drawn.

II. Schematic Description of the Film-Cooling Configurations

The principle flow features of the current supersonic film-cooling configurations are shown in Fig. 2. The origin of the coordinate

system is at the upper tip of the lip. In Fig. 2a, the lip-expansion fan and lip-shock wave occurring at the point of injection due to the finite thickness of the lip are illustrated. The lip-expansion fan and the shock wave emanating from the lower tip of the lip impinge upon the laminar slot boundary layer and cause a separation bubble. These waves are reflected and penetrate through the mixing layer and the free-shear layer. This is the configuration without any additional outer shock wave interacting with the cooling film, i.e., without any additional pressure gradient.

Figure 2b shows the configuration of the outer shock interacting with the cooling film. The shock/cooling-film interaction is located in the potential-core region. The incident shock wave is curved in the shear layer and mixing layer. It causes a laminar separation bubble undergoing transition. Because the injected film is a low supersonic flow at Mach 1.2, a subsonic region extends into the mixing layer far above the wall where the foot of the shock is perpendicular to the local flow direction.

Figure 2c shows the interaction of the outer shock and the cooling film to be located further downstream, i.e., in the boundary-layer region (Fig. 1). In this region, the mixing layer has reached the surface, and the shock foot occurs deeper in the mixing layer. The principal flow features (i.e., the compression and expansion waves and the reflected shock wave) resemble those of the shock/cooling-film interaction in the potential-core region in Fig. 2b. However, the mixing is already much further developed than in the configuration sketched in Fig. 2b such that the flow structure interacting with the incident shock is clearly different resulting in an altered cooling effectiveness.

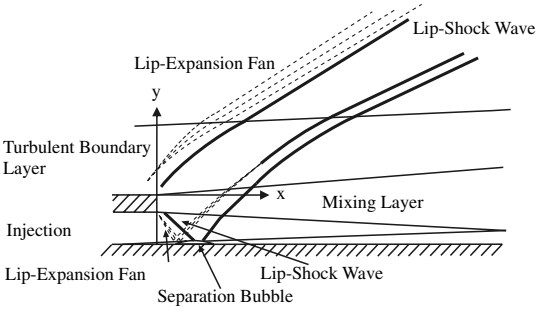

a) Flow features in the slot vicinity

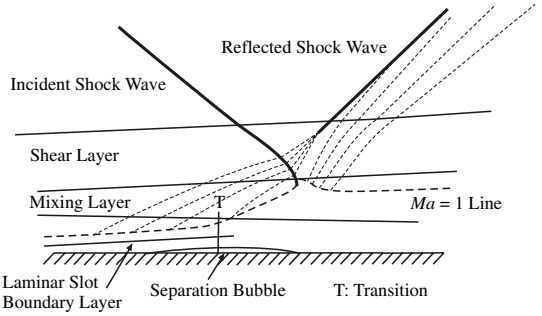

b) Shock/cooling-film interaction in the potential-core region

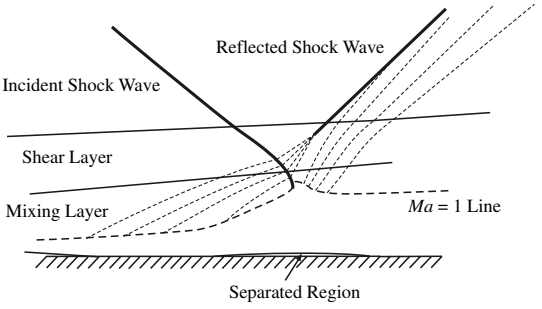

c) Shock/cooling-film interaction in the boundary-layer region

Fig. 2 Sketch of the flow features near the slot and at shock/cooling-film interaction in the potential-core region (case II) and in the boundary-layer region (case III).

III. Numerical Method

The flow structure of a shock interacting with free-shear layers, mixing layers, and laminar cooling flows is highly intricate because separation, transition, and reattachment occur. Previous numerical studies on film injection are primarily based on solutions of the RANS equations using, e.g., variations of the two-equation k–ε turbulence models [19,20]. In some of these RANS-based analyses, a satisfactory agreement with flowfield measurements such as the Mach number and temperature off the wall is achieved when using the turbulence model of So et al. [21]. Moreover, quite a discrepancy between different turbulence models is observed when, e.g., the predicted wall temperature distribution is compared. This variation can be expected because the mixing layer formation at the lip is characterized by strong nonequilibrium flow structures, which are poorly captured by RANS models [22].

For the accurate computation of the mixing layer development, which determines the cooling effectiveness, off-the-shelf zero-, one-, or two-equation turbulence models have to be extended to include the impact of the density ratio, the convective Mach number, changes in the turbulent Prandtl number, and laminar-turbulent transition. Regarding the simultaneous occurrence of these phenomena, no convincing RANS model is available [23], which is why a higher-fidelity turbulence modeling is used in the current study. That is, the turbulence modeling is based on the large-eddy simulation (LES) approach to solve the three-dimensional unsteady compressible Navier–Stokes equations.

The method possesses the following main features. The nonresolved subgrid scales are implicitly modeled by the monotone integrated LES approach introduced by Boris et al. [24]. The temporal approximation is based on an explicit five-step Runge–Kutta method at second-order accuracy. The inviscid terms are discretized by a modified version of the second-order mixed centered-upwind advective upstream splitting method [25]. The discretization of the viscous terms is done by a second-order centered approximation. The viscosity is evaluated using the power law $\mu/\mu_t = (T/T_t)^{0.72}$. The details of the flow solver are discussed in Meinke et al. [26], and the quality of its solutions is extensively validated for generic flow problems in [27] and turbulent film-cooling flows in [28,29]. Shock/boundary-layer interactions investigated in [30] show the convincing accuracy and convergence behavior of the current LES method in supersonic turbulent flows.

IV. Boundary Conditions and Computational Mesh

At the inflow of the film cooling domain shown in Fig. 3, the supersonic compressible turbulent boundary layer has to be accurately prescribed. This is a challenging problem in large-eddy simulations because instantaneous data for the flow variables are required. To avoid the costly computation of the complete spatially developing boundary layer, an independent rescaling simulation is used. In this simulation, which is performed simultaneously with the film-cooling simulation, an instantaneous boundary-layer

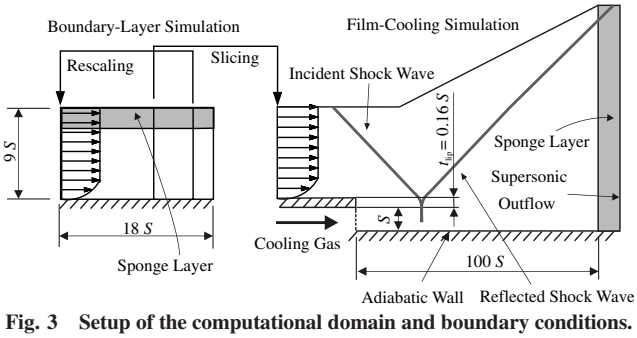

Fig. 3 Setup of the computational domain and boundary conditions.

distribution is generated by the rescaling method proposed by El-Askary et al. [30]. It generates an inflow distribution by rescaling the velocity and temperature field such that a prescribed boundary-layer thickness results. This rescaling method, the procedure of which is illustrated in Fig. 3, is a compressible extension of Lund et al.'s [31] approach, taking Mach number and temperature effects across the boundary layer into account. In each time step, the data of this additional flat plate simulation are inserted by a slicing technique into the computation of the film-cooling problem.

At the wall, no-slip and adiabatic conditions are used, and in the spanwise direction fully periodic boundary conditions are imposed. At the upper boundary, the inviscid freestream flow is prescribed. At the outflow, all variables are extrapolated. A sponge layer is used at the top of the rescaling domain and at the outflow of the film-cooling domain to damp any spurious oscillations. At the film-cooling slot, a laminar supersonic uniform-like velocity distribution is defined with thin compressible laminar boundary layers at the walls. The shock waves in the film-cooling domain are defined by the Rankine–Hugoniot relations such that, on the upper boundary, the flow variables satisfy the required shock angle and shock strength. Downstream of the shock wave, the computational domain is extended in the normal direction to ensure the reflected shock wave to exit the computational domain via the outflow boundary.

The computational grid consists of 33.8×10^6 points at a minimum wall resolution in inner coordinates of $\Delta x^+ = 20$, $\Delta y^+ = 0.5$, $\Delta z^+ = 10$ in the streamwise, wall-normal, and spanwise directions. In the streamwise and spanwise directions, an equidistant mesh is used. The computational domains sketched in Fig. 3 have a spanwise extension of $L_z/S = 4.4$, where the reference length S is the slot height. The lip thickness t_{lip} is $0.16S$.

The statistics is determined after a computational time of at least $t/\text{Su}_\infty = 370$ is reached. The computations are temporally averaged over a period of $\Delta t/\text{Su}_\infty = 250$ using 500 samples of the flowfield. Additionally, the results are spanwise-averaged.

V. Details of the Test Case

The injection condition and the freestream flow configuration are the same as in the experiments by Juhany et al. [7], who used a blowdown wind tunnel to accelerate air from ambient conditions to a freestream Mach number of $Ma_\infty = 2.44$. The boundary-layer thickness at the tip of the lip is given by $\delta/S = 2.27$. The section downstream of the injectant slot was made of the low-heat-conductivity alloy Hastelloy-X. The plate was instrumented with thermocouples and pressure tabs. The total test-section length, spanwise distance, and height are $266.6S$, $43.3S$, and $17.3S$. Because of the small wind-tunnel height, an adverse-pressure gradient existed in the test section. The cooling flow was injected through a nozzle where the upper wall has an angle of 10 deg. In another study, Juhany and Hunt [12] obtained pitot probe profiles for isoenergetic and heated injection cases and investigated the effect of shock-waves impinging upon the boundary-layer region for heated and isoenergetic injection conditions. However, no flowfield measurements at the shock interaction region are provided, the geometry of the wedge deflecting the flow is not given, and an expansion fan impinges upon the cooling flow immediately downstream of the shock wave. Therefore, the Juhany and Hunt data only without shock interaction are used for comparison.

VI. Flow Configuration

The parameters of the five supersonic cooling configurations are summarized in Table 1. Cases I, Ia, and Ib are the reference cases without an outer shock wave impinging upon the cooling film. The solutions are compared with experimental data from [7,12] in Sec. VII.A.2. At cases I and Ia, the influence of the incoming boundary-layer thickness on the cooling effectiveness is studied. Juhany et al. [7] state the boundary-layer thickness to be $\delta/S = 2.27$. However, matching the inflow profile of the current LES with the profile obtained from Juhany and Hunt [12] indicates the boundary-layer thickness at the lip to be $\delta/S = 1.4$. At case Ib, the correct

Table 1 Flow parameters

Case	δ/S	Ma_i	$T_\text{ti}/T_{t\infty}$	$M = \rho_\text{i} u_\text{i}/\rho_\infty u_\infty$	β, deg	Ma_3	x_imp/S
I	2.27	1.2	0.8	0.4	0	2.44	
Ia	1.4	1.2	0.8	0.4	0	2.44	
Ib	1.4	1.28	1	0.39	0	2.44	
II	2.27	1.2	0.8	0.4	5	2.04	17
III	2.27	1.2	0.8	0.4	5	2.04	40

prediction of the flowfield is validated by comparing numerical pitot pressure profiles with the experiments of Juhany and Hunt. In case II, the outer shock wave interacts with the potential-core region of the injected coolant, and case III is defined by the outer shock wave impinging upon an almost fully developed boundary layer, i.e., the interaction is far downstream of the potential-core of the cooling jet.

The Reynolds number $Re_\infty = u_\infty S/\nu_\infty$, based on the slot height, the freestream velocity u_∞, and the kinematic viscosity of the freestream, is $Re_\infty = 13,500$. The Reynolds number of the slot flow $Re_\text{i} = u_\text{i} S/\nu_\text{i}$, based on the centerline velocity and kinematic viscosity of the slot, is $Re_\text{i} = 4600$ (cases I, Ia, II, and III) and $Re_\text{i} = 3845$ (case Ib). In the four cooling configurations at cases I, Ia, II, and III, the injection conditions are kept constant at the same blowing rate M, total temperature ratio $T_\text{ti}/T_{t\infty}$, and injection Mach number Ma_i. The blowing rate M is computed by the integrated mass flow through the slot divided by the slot height S. At the cooling slot, two thin compressible boundary layers for both walls are assumed with a boundary-layer thickness of $\delta = 0.067S$, and the injection pressure matches the freestream pressure p_∞. Note that the slight inclination of the upper wall of the slot in the experiment of Juhany et al. [7] results in a radial flow, which is not considered in the current study. The shock waves are generated by a flow deflection of $\beta = 5$ deg and impinge 17 (case II) or 40 (case III) slot heights downstream of the slot in an inviscid unperturbed flowfield. The Mach number downstream of the reflected shock is $Ma_3 = 2.04$.

VII. Results

In the following, first a validation of the turbulent inflow distributions is presented. Next, the supersonic film-cooling configurations cases I, Ia, and Ib are considered by comparing numerically obtained cooling effectiveness values and pitot pressure profiles with experimental data of Juhany et al. [7] as well as Juhany and Hunt [12]. Then, the flow characteristics of supersonic cooling films interacting with shock waves, i.e., cases II and III, are presented followed by the analysis of the instantaneous flowfields. Subsequently, the impact of shocks and their impingement location on the cooling effectiveness, the mean flowfield including turbulence statistics, and the turbulent transport of heat and momentum are discussed.

A. Supersonic Film Cooling (Cases I, Ia, and Ib)

This section is divided into two parts. First, the validation of the rescaling method for the turbulent inflow distribution is presented, and then the results of the no-shock configurations (cases I, Ia, and Ib) are validated together with an in-detail discussion of the flowfield.

1. Validation of the Rescaling Method

The freestream Mach number is $Ma_\infty = 2.44$ and the freestream Reynolds number based on the momentum thickness of the boundary layer at $x/S = -4$, i.e., four injection gaps upstream of the lip tip, is $Re_\theta = 2236$ at cases I, II, and III. The profile of the streamwise velocity component nondimensionalized by the friction velocity u_τ and scaled by the van Driest transformation is compared in Fig. 4 with theoretical data and a numerical solution from Urbin and Knight [32] at $Ma = 3$. The logarithmic region compares well with the law of the wall $u^+ = 1/0.41 \cdot \ell_n\, y^+ + 5.2$ and the profile obtained from the LES of Urbin and Knight [32]. The difference in the wake is due to the difference in the freestream Mach number. The distributions of the Reynolds stress components scaled by the ratio of the local

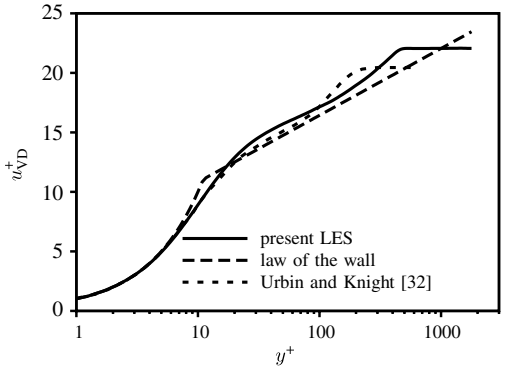

Fig. 4 Van Driest transformed velocity profiles in wall units.

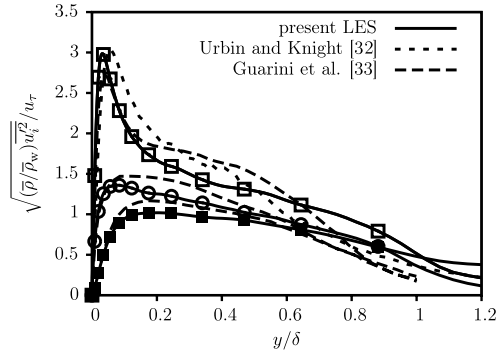

Fig. 5 The rms velocity profiles vs y/δ, □ streamwise velocity component, ○ spanwise velocity component, ■ wall-normal velocity component.

density $\bar{\rho}$ to the wall density $\bar{\rho}_w$ and the friction velocity versus the wall-normal distance are shown in Fig. 5. A qualitatively and quantitatively satisfactory agreement can be observed with the direct numerical simulation of Guarini et al. [33] at $Ma = 2.5$ and $Re_\theta = 1577$ and the LES of Urbin and Knight [32]. This convincing match of the data is also confirmed by the distribution of $\overline{u'v'}/u_\tau^2$ as a function of the wall-normal distance in Fig. 6.

In film-cooling flows, the ratio of the turbulent eddy viscosity and diffusivity plays an essential role as far as the mixing and as such the cooling effectiveness is concerned. This ratio is expressed by the turbulent Prandtl number, which is defined for compressible flows [33] by

$$Pr_t = \frac{\overline{\rho u'' v''}(\partial \tilde{T}/\partial y)}{\overline{\rho v'' T''}(\partial \tilde{u}/\partial y)} \tag{1}$$

Note that, in most turbulence models, Pr_t is assumed constant. The distributions in Fig. 7 show that this assumption is quite crude because pronounced variations occur in the boundary layer. The good comparison of the present results and the findings from Guarini et al. [33] also indicates the convincing quality of the current inflow data. Note that Eq. (1) results in an infinite or zero turbulent Prandtl number at the wall and at the boundary-layer edge, where the Reynolds stress, turbulent heat flux, and gradients are close to zero.

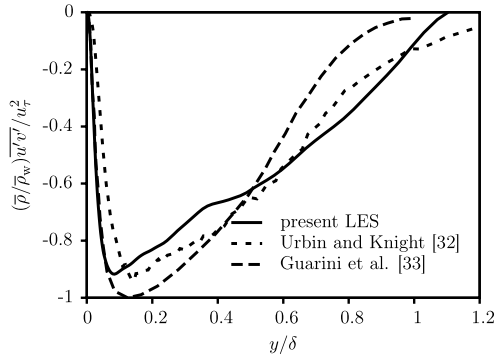

Fig. 6 $\overline{u'v'}$ scaled by u_τ^2 and $\bar{p}/pw$ vs y/δ.

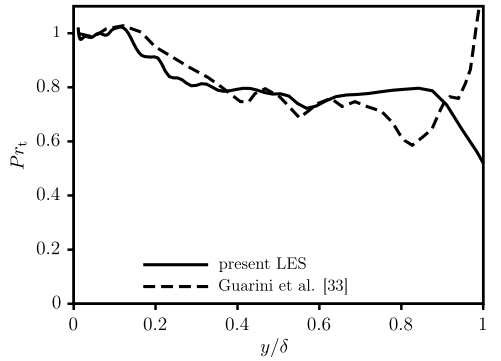

Fig. 7 Turbulent Prandtl number vs y/δ.

The influence of the incoming boundary-layer thickness on the adiabatic cooling effectiveness is studied in cases I and Ia because Juhany et al. [7] report a larger boundary-layer thickness ($\delta/S = 2.27$) than that ($\delta/S = 1.4$) obtained from pitot pressure measurements of the same experiment [12]. Figure 8 shows the good match of the inflow profile at cases Ia and Ib with the measurements of Juhany and Hunt at $x/S = 0$ at a boundary-layer thickness of $\delta/S = 1.4$.

2. *No-Shock Reference Configurations*

The adiabatic cooling effectiveness,

$$\tilde{\eta} = \frac{\tilde{T}_{aw} - T_{r\infty}}{T_{ri} - T_{r\infty}} \tag{2}$$

is determined for the no-shock reference configurations (cases I and Ia) to validate the current film-cooling computations. In Fig. 9, the

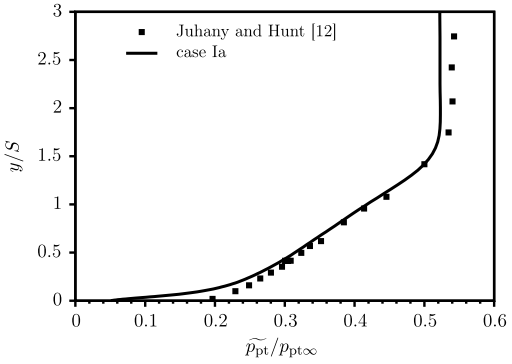

Fig. 8 Comparison of the numerical pitot pressure profile to the experiment of Juhany and Hunt [12] at the slot at $x/S = 0$.

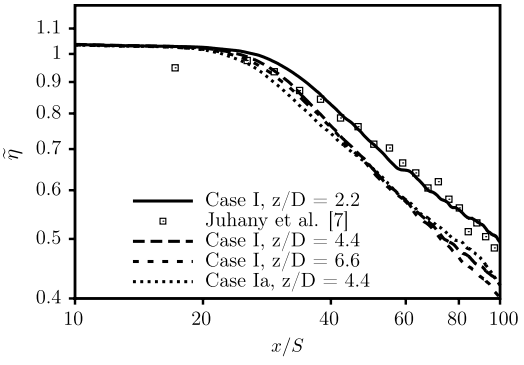

Fig. 9 Comparison of numerical cooling effectiveness values with the experiment of Juhany et al. [7].

numerically obtained cooling effectiveness values are compared with the experimental data of Juhany et al. [7]. The result of the sensitivity study of the spanwise domain extension shows that the cooling effectiveness distribution converges at a spanwise domain size of $z/S = 4.4$. Therefore, all simulations in the current study are performed at this spanwise domain size. The length of the potential-core region, where the cooling effectiveness is close to unity, is correctly captured at this spanwise domain. The gradient of the cooling effectiveness in the wall-jet and boundary-layer region is overpredicted compared to the experiment of Juhany et al. [7]. This overprediction is due to several factors. In the experiment, the recovery temperatures were measured and were higher than those obtained from empirical relations [7]. This indicates that some thermal conduction most likely occurred in the experiment. However, in the current simulations, the reference recovery temperatures in Eq. (2) are obtained by

$$T_r = T_e\left(1 + r\frac{\gamma - 1}{2}Ma_e^2\right) \tag{3}$$

using the appropriate temperature at the boundary-layer edge. They do match the wall temperatures in the current simulations. The recovery factor is evaluated using $r = \sqrt{Pr}$ for the laminar slot boundary layer and $r = \sqrt[3]{Pr}$ for the turbulent freestream boundary layer. Furthermore, the low height of the wind tunnel of $y/S = 17.3$ caused an adverse-pressure gradient and led to the reflection of the lip shock and expansion waves at the upper wall, which is not considered in the current simulations. Because Juhany et al. [7] give a boundary-layer thickness at the lip of $\delta/S = 2.27$ but pitot probe measurements of Juhany and Hunt [12] indicate the boundary-layer thickness to be $\delta/S = 1.4$, the influence of the thickness of the incoming boundary layer is studied at cases I and Ia. Figure 9 shows no significant differences, and hence the shock/cooling-film interaction cases II and III are performed at $\delta/S = 2.27$. Cary and Hefner [3] found that the ratio of the incoming boundary-layer thickness to the slot height has no significant effects on the adiabatic cooling effectiveness. The new results extend the findings of Cary and Hefner from ratios of $\delta/S = 31, 10.7, 4.6$ to the current δ/S ratios of cases I and Ia.

To validate the predictions of the current computational method, off-the-wall pitot pressure profiles of the no-shock case Ib are compared to the data by Juhany and Hunt [12]. The numerical profile, shown in Fig. 10, matches the experimental profile at $x/S = 3$, $-1.16 \le y/S \le 0$, which shows the correct prescription of the slot flow in the simulation. The shear-layer prediction at $x/S = 3$, $0 \le y/S < 1.4$ agrees with the measurements, and some deviations occur at $y/S = 1.4$ due to the lip expansion fan and shock wave. The profiles further downstream show a good agreement of the current LES solution and the experiments. The slight deviation at $x/S = 58$, $1 \le y/S \le 2$ is probably caused by the reflection of the expansion fan and the shock system originating at the slot at the upper wall of the wind tunnel.

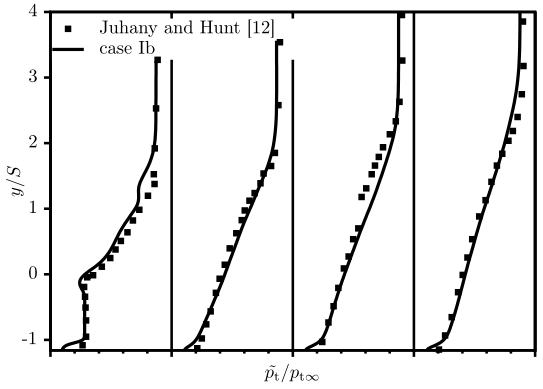

Fig. 10 Comparison of numerical pitot pressure profiles to the experiment of Juhany and Hunt [12] at the streamwise positions $x/S = 3, 41, 58, 96$; grid spacing is $\Delta\tilde{p}_{pt}/p_{pt\infty} = 0.6$.

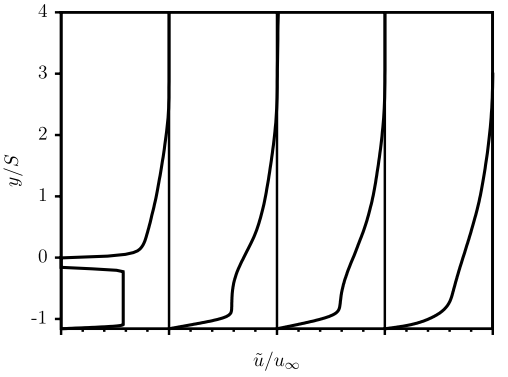

Fig. 11 Velocity profiles at $x/S = 0, 10, 15, 30$ for case I; grid spacing is $\Delta\tilde{u}/u_\infty = 1$.

The streamwise velocity profiles at case I are used to identify the various flow regions defined in Fig. 1, i.e., the potential-core, the wall-jet, and the boundary-layer region. Figure 11 shows the development of the velocity profile of the injected fluid. The inflow distribution shows a constant velocity at $x/S = 0$, $-1.16 \le y/S \le -0.16$. Further downstream, this constant streamwise velocity area shrinks and vanishes near $x/S = 15$, marking the location of the end of the potential core. Subsequently, in the wall-jet region at $15 \le x/S \le 30$, the mixing of the cooling jet and the freestream flow forms a turbulent boundary-layer profile, which defines the beginning of the boundary-layer region.

The temperature profiles in Fig. 12 confirm the identification of the flow regions defined by velocity profiles. At the tip of the lip $x/S = 0$, $y/S = 0$, the high temperature of the fluid at the wall is evident. Further downstream at $x/S = 10$, $y/S = 0$, the temperature is decreased by the cooling flow and by the strong acceleration of the viscous sublayer emanating from the freestream boundary layer. At the end of the wall-jet region $x/S = 30$, a boundary-layer-like temperature profile has formed.

B. Shock/Cooling-Film Interaction (Cases II and III)

In the following, cases II and III (i.e., with shock/cooling-film interaction) are discussed to evidence the impact of the shock waves on the cooling effectiveness and turbulent thermal transport.

1. Flow Characteristics of Supersonic Film Cooling with Shock Waves

The flow structure in supersonic film cooling is illustrated by numerical schlieren images in Figs. 13 and 14. Figure 13 evidences the flowfield for case II, i.e., the interaction of the incident shock occurs at the end of the potential core, and Fig. 14 shows the flow structure for case III, where the interaction of the shock wave with the wall-bounded shear layer occurs further downstream. In either case, a highly intricate wave pattern is observed, the details of which are sketched in Fig. 2. In Fig. 13, the incoming turbulent boundary layer indicated by light gray contours (point a) is deflected toward the wall

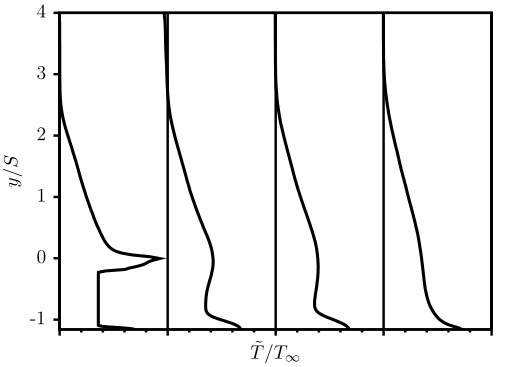

Fig. 12 Static temperature profiles at $x/S = 0, 10, 15, 30$ for case I; grid spacing is $\Delta\tilde{T}/T_\infty = 1$.

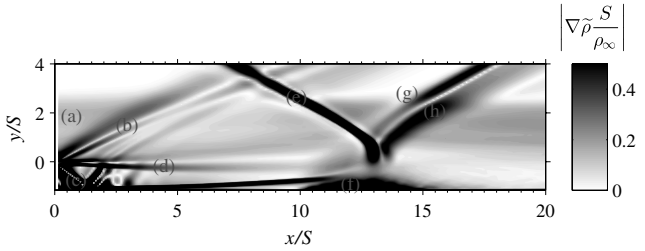

Fig. 13 Numerical schlieren image of the temporal and spanwise-averaged density gradient modulus in wall-normal and streamwise directions for case II; for explanation of points a–h, see text.

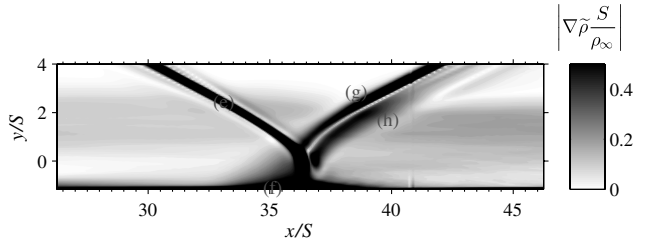

Fig. 14 Numerical schlieren image of the temporal and spanwise-averaged density gradient modulus in wall-normal and streamwise directions for case III; incident shock wave (e), separation bubble (f), shock wave (g), expansion fan (h).

by an expansion fan emanating from the upper tip of the lip (point b), which is followed by a shock wave to readjust the flow direction to be parallel to the surface. At the lower tip of the lip at $y/S \leq -0.16$, another expansion fan (point c) occurs, which is reflected at the laminar slot boundary layer on the surface and interacts with the mixing layer, which is generated in the wake of the lip. The lower part of the mixing layer (point d) separates the film-cooling flow from the freestream. Further downstream, the incident oblique shock wave (point e) enters the free-shear layer and the laminar boundary layer to form a strongly curved wave region and to cause a separation bubble (point f). The incident shock wave is reflected (point g), and the convex shape of the separation generates an additional expansion fan (point h).

The numerical schlieren image in Fig. 14 shows the foot of the incident shock wave (point c) to penetrate deeper into the boundary layer. This causes a smaller separation bubble, i.e., the detached flow region is shorter and thinner. Therefore, the displacement of the flow by the separation bubble is smaller.

To clearly locate the separation bubble and to define its extent, the skin-friction coefficient distribution is shown in Fig. 15 for cases II and III. It is evident that the case II bubble is larger ($L_{sep}/S = 7.6$) than the case III bubble ($L_{sep}/S = 1.5$) due to the laminar character of the wall-bounded shear layer at case II. The wall-pressure distributions in Figs. 16 and 17 indicate a slight plateau region at

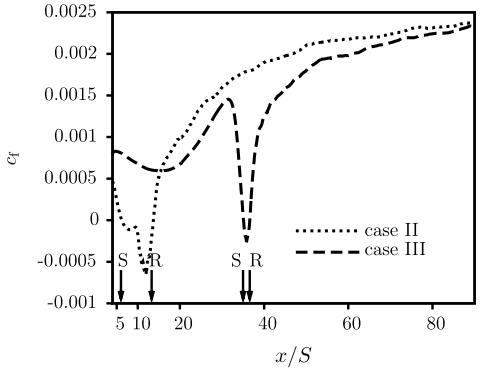

Fig. 15 Skin-friction coefficient distribution for the cases II and III; separation (S) and reattachment (R) are indicated by arrows.

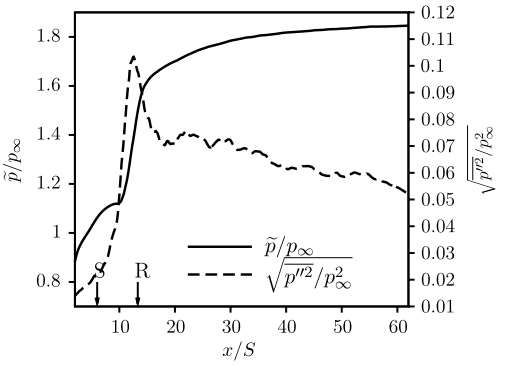

Fig. 16 Mean wall pressure and rms of wall-pressure fluctuations for case II; separation (S) and reattachment (R) are indicated by arrows.

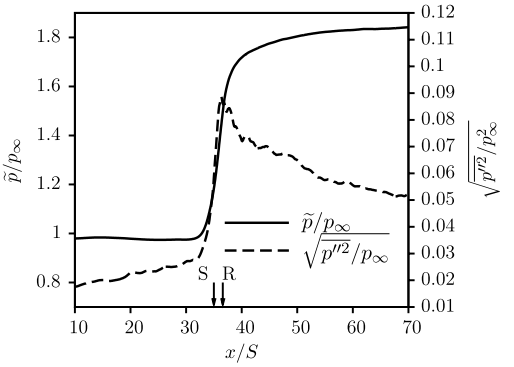

Fig. 17 Mean wall pressure and rms of wall-pressure fluctuations for case III; separation (S) and reattachment (R) are indicated by arrows.

case II, whereas at case III only a strong pressure rise is observed. The occurrence of the interaction of the shock wave with the cooling film in the potential-core region generates not only a larger separation bubble but also a detachment that is much more unsteady than the interaction with a fully turbulent boundary layer observed at case III. The rms distribution of the pressure fluctuations at case II in Fig. 16 possesses a much more pronounced peak than the distribution at case III in Fig. 17. To be more precise, the case III peak is 14.5% less than that at case II.

2. *Instantaneous Flowfield*

In Fig. 18, the shock wave impinging upon the potential-core region is visualized by λ_2 contours [34] with mapped-on Mach number distribution. The shock waves are evidenced by gray contours of the velocity divergence $\partial u_i/\partial x_i \cdot S/u_\infty$. The potential-core region (i.e., the region without any vortices) is located underneath the free-shear layer. The interaction of the oblique shock wave with the shear layer causes an immediate transition of the

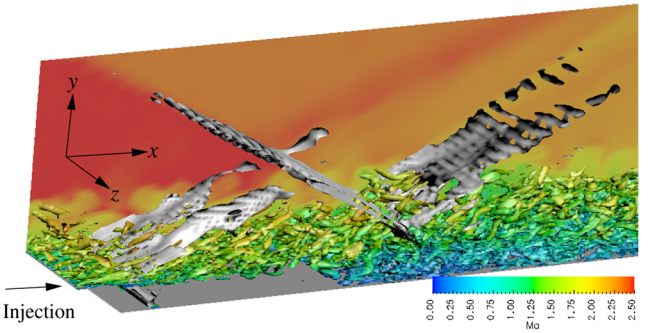

Fig. 18 Flow structures of case II visualized by the λ_2 criterion with mapped-on Mach number; contours of shocks and expansion fans at $\partial u_i/\partial x_i \cdot S/u_\infty = -0.4$.

laminar slot boundary layer in the separation bubble. Figure 19 illustrates the flowfield for case III. The laminar slot boundary layer has already undergone transition, and the shock impinges upon the turbulent boundary-layer region. Even this qualitative image of the flow structure shows the pronounced thickening of the wall-bounded shear layer occurring at case II compared to the weaker impact of the shock impingement at case III.

3. *Cooling Effectiveness*

The adiabatic cooling effectiveness η [Eq. (2)] is determined for the three cooling configurations to investigate the impact of the shock waves and the impingement location on the cooling effectiveness. Figure 20 shows the numerically obtained cooling effectiveness values for the three cooling configurations. At case II, the potential-core region is reduced to $x/S = 13$ because the incident shock wave destabilizes the laminar slot boundary layer and excites laminar-turbulent transition, resulting in a more-pronounced mixing with the shear layer, which emanates from the lip. That is, the drop in cooling effectiveness has three reasons. The first is the transition of the laminar slot boundary layer. This leads to an increase of the adiabatic wall recovery temperature. The second reason is due to the reduced local Mach number downstream of the shock impingement that also results in an increased wall recovery temperature. This issue also was pointed out by Kanda et al. [35]. The third reason is the enhanced momentum transfer and the resulting pronounced mixing between the cooling flow and the freestream, which is analyzed in detail next. At case III, the shock interaction is located further downstream in the fully turbulent boundary-layer region, and the cooling effectiveness is immediately reduced downstream of the shock-impingement location. Unlike cases I and II, the cooling effectiveness possesses a steeper streamwise slope, i.e., a more drastic variation of the cooling effectiveness is observed. To evidence the various gradients at cases I, II, and III, the cooling effectiveness in the boundary-layer region and/or just downstream of the shock-impingement location is approximated by

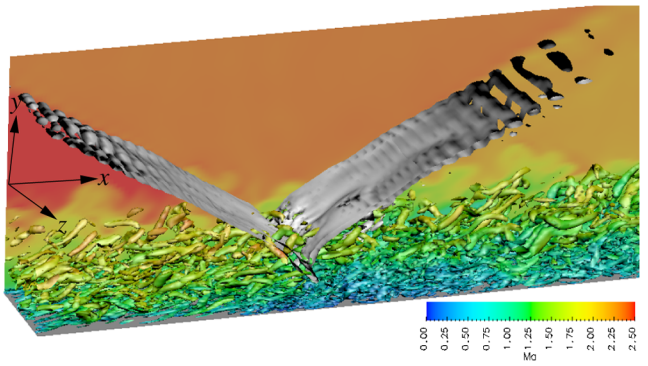

Fig. 19 Flow structures of case III visualized by the λ_2 criterion with mapped-on Mach number; contours of shocks and expansion fans at $\partial u_i/\partial x_i \cdot S/u_\infty = -0.4$.

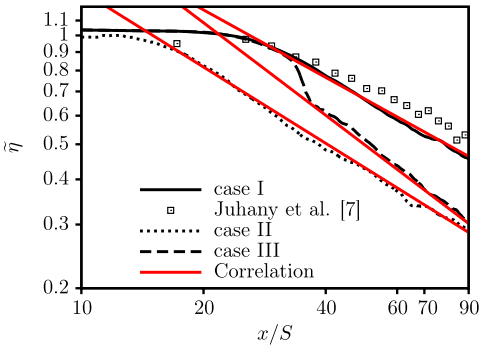

Fig. 20 Numerical and experimental adiabatic cooling effectiveness η.

Table 2 Adiabatic cooling effectiveness exponent m in $\eta = (x/r)^m$.

Case	m
I	−0.62
II	−0.7
III	−0.85

$$\eta = (x/r)^m \tag{4}$$

Table 2 lists the exponents m of the current cooling configurations, showing that it is highest at case III. That is, it is the interaction of the turbulent boundary layer and the shock wave that leads to stronger mixing of the two flows in the boundary-layer region. Further downstream of the interaction region, the excitation of the mixing through the shock impingement decreases. It is shown in Fig. 21 that this results in an asymptotic approximation of the freestream recovery wall temperature in all cases at increasing downstream distance from the slot.

Figure 21 also evidences a temperature drop close to the lip. This is caused by the expansion fan at the lower tip of the lip, and it is also the reason for the initial cooling effectiveness values in Fig. 20 to be slightly above unity.

Another important observation is the fluctuation of the wall temperature in the turbulent boundary layer. Frequently changing temperatures have to be taken into account in the design process of, say, the combustion chamber, to avoid thermal fatigue of the wall material or local hot spots that exceed the upper limit of the wall material. To discuss the impact of wall temperature oscillations, the distribution of the fluctuating cooling effectiveness,

$$\sqrt{\overline{\eta''^2}} = \frac{\sqrt{\overline{T''^2_{\mathrm{aw}}}}}{T_{\mathrm{r}\infty} - T_{\mathrm{ri}}} \tag{5}$$

at case II is shown in Fig. 22 together with the temporal and spanwise-averaged adiabatic cooling effectiveness. It is evident that, near the reattachment point, the fluctuating cooling effectiveness $\sqrt{\overline{\eta''^2}}$ possesses a pronounced peak. Further downstream, the fluctuating cooling effectiveness still has such a high level, i.e., on the order of 10^{-1}, that these oscillations cannot be neglected. In Fig. 23 at case III, the peak of $\sqrt{\overline{\eta''^2}}$ is 13% lower than at case II; however, the same fluctuation level is reached downstream of the shock impingement.

The reason for these high fluctuations near the reattachment point at case II is revealed by analyzing at this point, i.e., at $x/S = 12.01$, the temporal development of the adiabatic cooling effectiveness, which is shown in Fig. 24 for the centerline plane. At $t_2/(S/u_\infty) = 593.5$ and $t_3/(S/u_\infty) = 679.5$, the cooling effectiveness is as low as 0.6, although the averaged cooling effectiveness is $\eta = 1$. The flowfield at the marked maxima and minima, i.e., at different time steps, is shown using streamlines and contours of the instantaneous

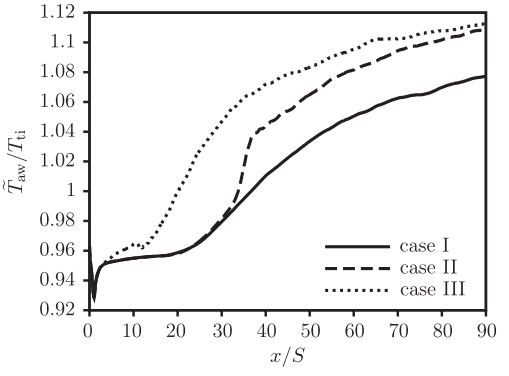

Fig. 21 Adiabatic wall temperature vs distance.

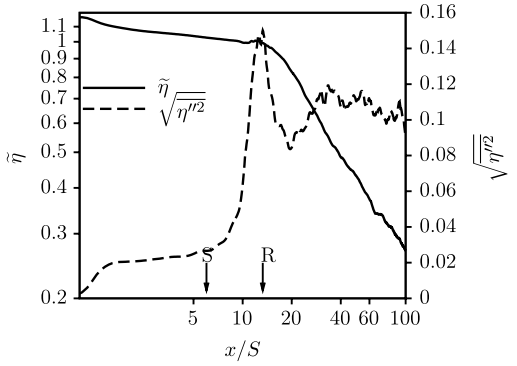

Fig. 22 Mean and rms adiabatic cooling effectiveness values at case II; separation (S) and reattachment (R) are indicated by arrows.

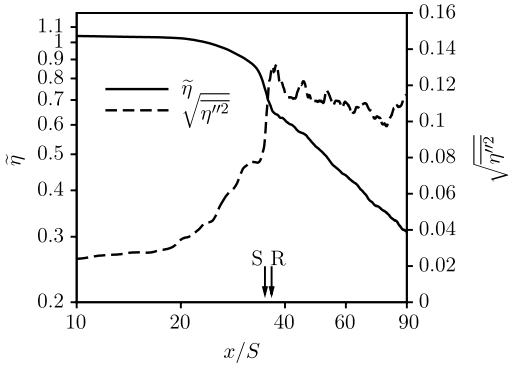

Fig. 23 Mean and rms adiabatic cooling effectiveness values at case III; separation (S) and reattachment (R) are indicated by arrows.

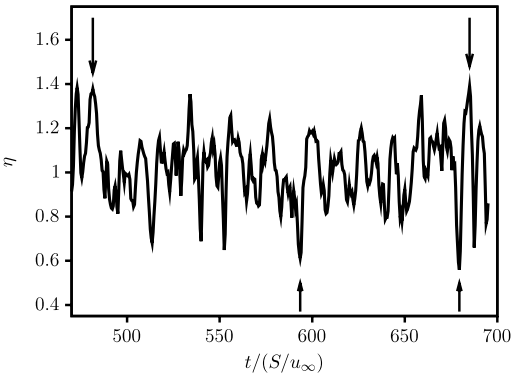

Fig. 24 Cooling effectiveness vs time at the point of maximum fluctuations $x/S = 12.01$ for case II.

total temperature in Fig. 25. In Fig. 25a, a vortex close to the mean reattachment point occurs. The near-wall flow is reversed, and the instantaneous total temperature is reduced to 0.7 in the recirculation region, yielding a maximum cooling effectiveness. In Fig. 25b, the flowfield is shown for the minimum cooling effectiveness at $t_2/(S/u_\infty) = 593.5$, revealing an attached flow with high levels of total temperature of approximately 0.8. Attached flow and a high instantaneous total temperature value close to the wall are also evident in Fig. 25c, resulting in a reduced cooling effectiveness. In Fig. 25d, the flow is again separated, which is why a high temporal cooling effectiveness is observed. These instantaneous illustrations of the flowfield reveal minimum cooling effectiveness to occur when the flow reattaches and maximum cooling effectiveness to be associated with a locally reversed flow and low total temperature values.

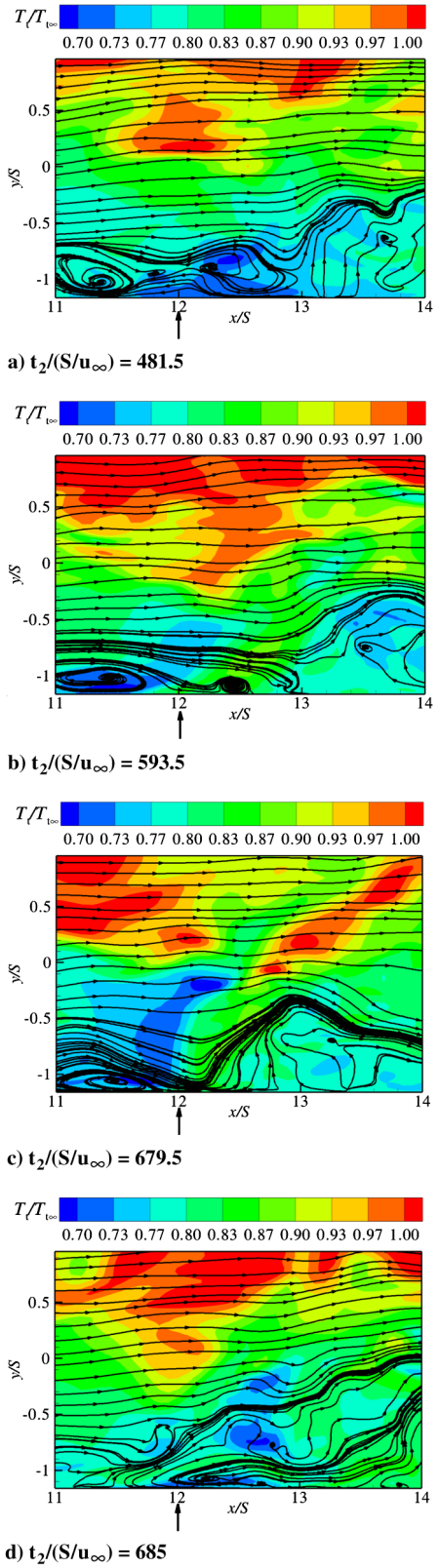

Fig. 25 Instantaneous total temperature contours and streamlines in the x, y plane at $z/S = 2.2$ for case II; the arrow indicates the point of maximum cooling effectiveness fluctuations.

4. Mean Flowfield

The dimensionless fluid temperature,

$$\Theta = \frac{\tilde{T}_t - T_{t\infty}}{T_{\mathrm{ti}} - T_{t\infty}} \tag{6}$$

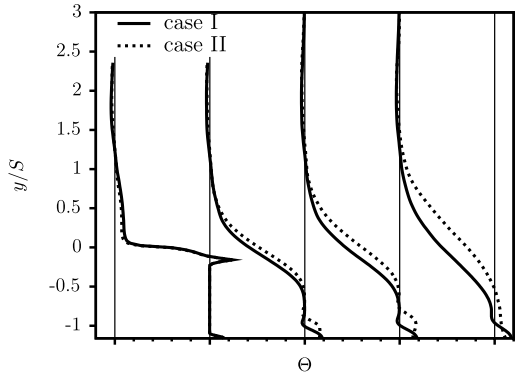

a) x/S = 0, 8, 10, 15, cases I and II

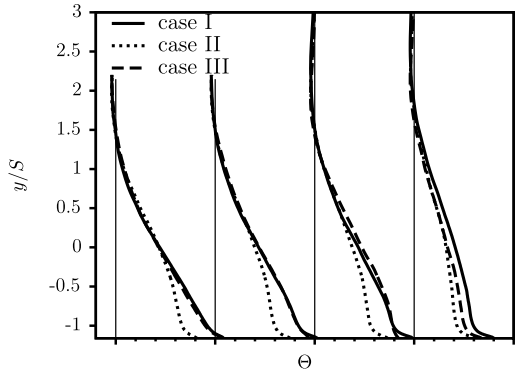

b) x/S = 30, 36, 40, 60, cases I, II, and III

Fig. 26 Dimensionless fluid temperature; grid spacing is $\Delta\Theta = 1$.

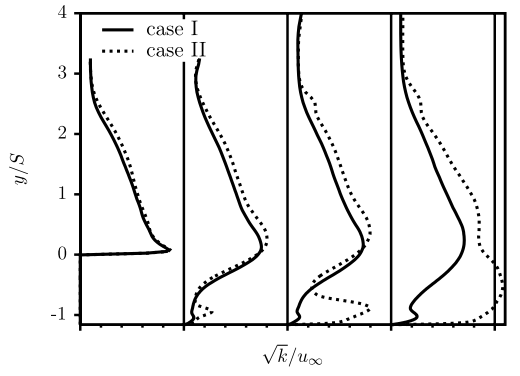

a) x/S = 0, 8, 10, 15, cases I and II

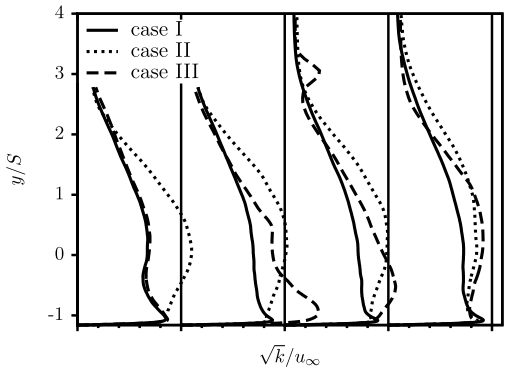

b) x/S = 30, 36, 40, 60, cases I, II, and III

Fig. 27 Turbulent kinetic energy profiles; grid spacing is $\Delta\sqrt{k}/u_\infty = 0.1$.

is evaluated downstream of the cooling flow injection to assess the momentum transfer and mixing of the coolant and the freestream. The definition of the dimensionless fluid temperature Θ is similar to the definition of the cooling effectiveness η, but the total temperatures of the coolant T_{t_i} and the freestream T_{t_∞} are used as reference temperatures instead of the recovery temperatures. That is, the dimensionless cooling temperature is 1 in the cooling flow and 0 in the freestream. In Fig. 26, the streamwise development of the dimensionless fluid temperature is shown. At case I, the mixing layer downstream of the lip exists at $x/S = 8, -0.5 \le y/S \le 0.5$, where Θ varies between 1 and 0. This mixing layer grows in the streamwise direction and merges with the laminar slot boundary layer at $x/S = 30$. At case II, the shock wave, which interacts with the wall-bounded flow at the end of the potential core, leads to a separation bubble being illustrated by the stronger displacement of the Θ profiles at $x/S = 10$ and 15. Downstream of the reattachment at $x/S = 30$, the dimensionless fluid temperature near the wall is decreased compared to case I, indicating stronger mixing of the two flows. This reduced Θ distribution extends through $x/S = 60$, where the profile resembles that of case I. The case III distribution shows a similar, somewhat weaker increase of Θ at $x/S = 40$ than the case II distribution at $x/S = 15$, which is due to the smaller separation. Downstream of the shock-impingement location at $x/S = 60$, the dimensionless fluid temperature is reduced by intense mixing. The temperature distribution is slightly higher than that of case II and somewhat smaller than that of case I.

5. *Turbulence Statistics*

The impact of the shock waves on the turbulence in the near-wall region is analyzed by the turbulent kinetic energy (TKE):

$$k = \frac{1}{2}(\overline{u''^2} + \overline{v''^2} + \overline{w''^2}) \tag{7}$$

High TKE values also mean intense mixing. In Fig. 27a, a slow rise of TKE due to the growing wall-bounded and free-shear layer is evident at case I. The shock wave impingement at case II causes a drastic increase of TKE to 0.1 in the near-wall layer at $x/S = 10$. The location of the peak is shifted off the wall at larger downstream distances, which is consistent with the stronger reduction of Θ in this region compared to the case I solution. At case I, the TKE peaks close to the wall in the boundary-layer region. Note that Fig. 27b evidences at case II the turbulent kinetic energy at this wall-normal distance to be reduced downstream of the shock. Case III shows the same behavior, i.e., the maximum TKE level moves off the wall at a larger streamwise location.

6. *Turbulent Transport of Heat and Momentum*

The cooling effectiveness gradient listed in Table 2 for case III is higher than for cases I and II. This means there is an increased transport of heat and momentum toward the wall. To further analyze this observation, the transport equation of the mean total temperature $T_t = T + u_i u_i/(c_p 2)$ in a zero-pressure-gradient boundary layer at small turbulent Mach number $Ma_t \ll 1$ is considered:

$$\bar{\rho}\,\tilde{u}\frac{\partial \tilde{T}_t}{\partial x} + \bar{\rho}\,\tilde{v}\frac{\partial \tilde{T}_t}{\partial y} = \frac{\partial}{\partial y}\left(\frac{\bar{\mu}}{Pr}\frac{\partial \tilde{T}_t}{\partial y} - \overline{\rho v'' T_t''}\right) \tag{8}$$

These conditions are approximately valid downstream of the shock impingement, where the turbulent Mach number is approximately $Ma_t = 0.2$. The wall-normal convective heat transport term,

$$f_v = \int_0^{\Delta y^*/S} \bar{\rho}\,\tilde{v}\,\tilde{T}_t/(\rho_\infty u_\infty T_{t_\infty})\,\mathrm{d}(y^*/S) \tag{9}$$

is integrated over the complete thickness of the freestream boundary layer to a wall-normal distance of $\Delta y^*/S = 3.83$. The quantity $\Delta y^*/S$ originates at the wall, i.e., $\Delta y^*/S = y/S - 1.16$. The value of this integral and the streamwise development are shown in Fig. 28. At case II, a large positive convective heat transport off the wall exists at position $x/S = 9$ due to the displacement of the separation bubble. Further downstream, a negative convective heat transport toward the wall occurs, which is reduced at increasing downstream distance. At

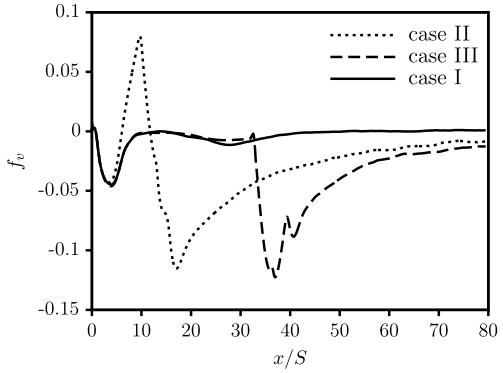

Fig. 28 Wall-normal convective heat transfer.

case III, there is a much weaker convective heat transport off the wall at $x/S = 32$ due to the smaller separation bubble. Downstream of the shock-wave impingement, the transport toward the wall is qualitatively like that at case II. The impact of the shock waves on the turbulent heat transport is illustrated in Fig. 29a. The maximum turbulent heat transport values toward the wall occur due to the shock impingement in the area $10 \leq x/S \leq 30$ at case II and within $40 \leq x/S \leq 60$ at case III. The latter result causes the stronger decrease of the cooling effectiveness at the wall and the dimensionless fluid temperature compared to cases I and II. Further downstream, the case II and III distributions approximate the case I profile.

It can be concluded that the turbulent thermal transport is significantly enhanced in the shock-impingement area. The larger cooling effectiveness gradient at case III is caused by the higher turbulent state of the boundary layer, which results in a greater temperature level in the near-wall flow upstream of the geometric shock-impingement point. The shock/boundary-layer interaction leads to a more pronounced mixing such that the already hotter fluid is transported toward the wall.

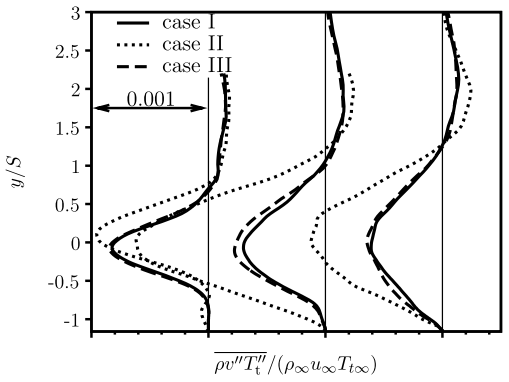

a) x/S = 10, 20, 30

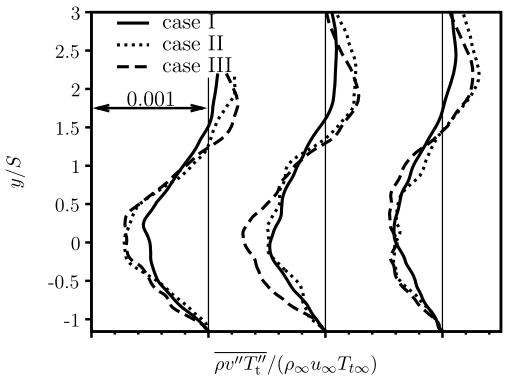

b) x/S = 40, 50, 60

Fig. 29 Nondimensionalized turbulent heat transfer for cases I, II, and III.

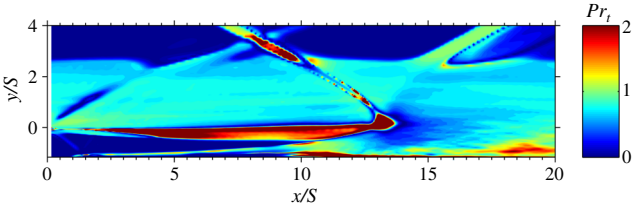

Fig. 30 Contours of the turbulent Prandtl number Pr_t for case II.

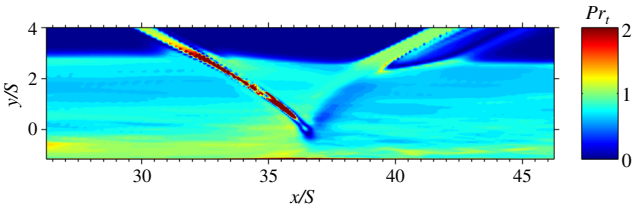

Fig. 31 Contours of the turbulent Prandtl number Pr_t for case III.

The turbulent Prandtl number is evaluated for cases II and III using the definition given in Eq. (1), which holds for turbulent boundary layers. Note that for, wall-jet and shock-interaction flows, other components of the Reynolds stress tensor and heat flux vector might play a role for the turbulent Prandtl number. However, other methods, e.g., computing the eddy viscosity by using the turbulent kinetic energy and Bradshaw's hypothesis, which uses the norm of the strain-rate tensor [36,37], did not provide significantly different results off the wall. Therefore, the current definition of the turbulent Prandtl number is used, which also yielded useful results in wall-jet and shock-interaction studies [38,39]. It is evidenced in Fig. 7 that, in turbulent boundary layers, Pr_t is close to 1 in the near wall region. The drastic deviations from this value in cases II and III are illustrated by contours in Figs. 30 and 31. The expansion fan originating at the upper part of the lip shown in Fig. 30 reduces the turbulent Prandtl number. In the potential-core region, the turbulent Prandtl number is zero and, in the mixing layer just above the potential core, values close to 2 occur. At increasing wall distance, Pr_t reaches values smaller than 1. At the foot of the shock wave, the Prandtl number is greater than 2, and further downstream values of approximately 0.5 occur. It is shown in Fig. 31 for case III that the effect of the incident shock wave is not as pronounced as at case II. The area of $Pr_t < 1$ is much smaller than at case II. Close to the wall at $x/S \geq 40$, $Pr_t \approx 1$ is observed. Hence, it can be concluded that the ratio of eddy viscosity and diffusivity is hardly affected at case III in the region where the cooling effectiveness gradient differs from that of cases I and II.

VIII. Conclusions

Large-eddy simulations of shock/cooling-film interaction were performed. The no-shock reference configuration (case I) resembled the Juhany et al. [7] problem, i.e., the laminar cooling flow at Mach 1.2 was injected into a supersonic turbulent boundary layer at Mach 2.44. The comparison of the numerical adiabatic cooling effectiveness with the experimental data from [7] correctly predicted the length of the potential-core region but overpredicted the cooling effectiveness decrease. Comparisons of pitot profiles at an additional isoenergetic injection condition (case Ib) showed a good match with the experiments of Juhany and Hunt [12]. The reference configuration (case I) was modified by considering oblique shock waves impinging upon the potential-core region (case II) and the boundary-layer region (case III). At the shock impact onto the potential core, the laminar slot boundary layer showed a significant separation region and an immediate transition to turbulence. The transition led to a pronounced mixing of the freestream and the cooling flow as well as a drastic decrease of cooling effectiveness. To be more precise, a decrease of cooling effectiveness by 36% was observed downstream of the shock-impingement point. In the separation bubble, strong cooling effectiveness fluctuations were found due to the highly unsteady reattachment. The shock wave

impinging upon the boundary-layer region (case III) resulted in a smaller separation region and 13% less peak cooling effectiveness fluctuations at a steeper slope in cooling effectiveness in the streamwise direction. The shock waves at both impingement positions led to higher turbulence and turbulent thermal transport toward the wall. The steeper slope of the cooling effectiveness in the streamwise direction occurred due to the more turbulent state of the boundary layer at the more downstream shock/boundary-layer interaction. The investigation shows that the closer the shock-impingement point is to the end of the potential core, the stronger the cooling effectiveness decreases. The turbulent Prandtl number showed significant variations from its standard value in turbulent boundary layers of 0.9. In the shear layer, values in the range of 0.7 were determined; in the shock-wave interaction region, the turbulent Prandtl number was above 2, and downstream of the shock the value decreased to 0.5.

Acknowledgments

The authors gratefully acknowledge the support by the German Research Foundation in the framework of the Research Training Group "Aero-Thermodynamic Design of a Scramjet Propulsion System for Future Space Transportation Systems" 1095 and the High Performance Computing Center Stuttgart.

References

[1] Anderson, J. D., "High-Temperature Gas Dynamics: Some Introductory Considerations", *Hypersonic and High-Temperature Gas Dynamics*, 2nd ed., AIAA, Reston, VA, 2006, pp. 449–461.

[2] Goldstein, R., Eckert, E., Tsou, F., and Haji-Sheikh, A., "Film Cooling with Air and Helium Injection Through a Rearward-Facing Slot into a Supersonic Air Flow," *AIAA Journal*, Vol. 4, No. 6, 1966, pp. 981–985. doi:10.2514/3.3591

[3] Cary, A., Jr., and Hefner, J., "Film-Cooling Effectiveness and Skin Friction in Hypersonic Turbulent Flow," *AIAA Journal*, Vol. 10, No. 9, 1972, pp. 1188–1193. doi:10.2514/3.50348

[4] Richards, B., and Stollery, J., "Laminar Film Cooling Experiments in Hypersonic Flow," *Journal of Aircraft*, Vol. 16, No. 3, 1979, pp. 177–181. doi:10.2514/3.58502

[5] Alzner, E., and Zakkay, V., "Turbulent Boundary-Layer Shock Interaction with and without Injection," *AIAA Journal*, Vol. 9, No. 9, 1971, pp. 1769–1776. doi:10.2514/3.49979

[6] Seban, R. A., and Back, L. H., "Velocity and Temperature Profiles in Turbulent Boundary Layers with Tangential Injection," *Journal of Heat Transfer*, Vol. 84, 1962, pp. 45–54. doi:10.1115/1.3684292

[7] Juhany, K., Hunt, M., and Sivo, J., "Influence of Injectant Mach Number and Temperature on Supersonic Film Cooling," *Journal of Thermophysics and Heat Transfer*, Vol. 8, No. 1, 1994, pp. 59–67. doi:10.2514/3.501

[8] Kamath, P., Holden, M., and McClinton, C., "Experimental and Computational Study of the Effect of Shocks on Film Cooling Effectiveness in Scramjet Combustors," 5th AIAA and ASME Joint Thermophysics and Heat Transfer Conference, Seattle, WA, AIAA Paper 1990-1713, June 1990.

[9] Coakley, T., "Turbulence Modeling Methods for the Compressible Navier–Stokes Equations," 16th AIAA Fluid and PlasmaDynamics Conference, Danvers, MA, AIAA Paper 1983-1693, July 1983.

[10] Olsen, G., Nowak, R., Holden, M., and Baker, N. R., "Experimental Results for Film Cooling in 2-D Supersonic Flow Including Coolant Delivery Pressure, Geometry, and Incident Shock Effects," 28th Aerospace Sciences Meeting, Reno, NV, AIAA Paper 1990-0605, Jan. 1990.

[11] Holden, M., Nowak, R., Olsen, G., and Rodriguez, K., "Experimental Studies of Shock Wave/Wall Jet Interaction in Hypersonic Flow," 28th Aerospace Sciences Meeting, Reno, NV, AIAA Paper 1990-0607, Jan. 1990.

[12] Juhany, K., and Hunt, M., "Flowfield Measurements in Supersonic Film Cooling Including the Effect of Shock-Wave Interaction," *AIAA Journal*, Vol. 32, No. 3, 1994, pp. 578–585. doi:10.2514/3.12024

[13] Kanda, T., Ono, F., Saito, T., Takahashi, M., and Wakamatsu, Y., "Experimental Studies of Supersonic Film Cooling with Shock Wave Interaction," *AIAA Journal*, Vol. 34, No. 2, 1996, pp. 265–271. doi:10.2514/3.13060

[14] Kanda, T., and Ono, F., "Experimental Studies of Supersonic Film Cooling with Shock Wave Interaction (2)," *Journal of Thermophysics and Heat Transfer*, Vol. 11, No. 4, 1997, pp. 590–592. doi:10.2514/2.6286

[15] Takita, K., and Masuya, G., "Effects of Shock Wave Impingement on Supersonic Film Cooling," *Journal of Spacecraft and Rockets*, Vol. 36, No. 4, 1999, pp. 602–604. doi: 10.2514/3.27207

[16] Peng, W., and Jiang, P.-X., "Influence of Shock Waves on Supersonic Film Cooling," *Journal of Spacecraft and Rockets*, Vol. 46, No. 1, 2009, pp. 67–73. doi:10.2514/1.38458

[17] Menter, F. M., "Zonal Two Equation k–ω Turbulence Models for Aerodynamic Flows," 23rd Fluid Dynamics, Plasmadynamics, and Lasers Conference, Orlando, FL, AIAA Paper 1993-2906, July 1993.

[18] Hyde, C., Smith, B., Schetz, J., and Walker, D. A., "Turbulence Measurements for Heated Gas Slot Injection in Supersonic Flow," *AIAA Journal*, Vol. 28, No. 9, 1990, pp. 1605–1614. doi:10.2514/3.25259

[19] Aupoix, B., Mignosi, A., Viala, S., Bouvier, F., and Gaillard, R., "Experimental and Numerical Study of Supersonic Film Cooling," *AIAA Journal*, Vol. 36, 1998, pp. 915–923. doi:10.2514/2.495

[20] Sarkar, S., "Numerical Simulation of Supersonic Slot Injection into a Turbulent Supersonic Stream," *International Journal of Turbo and Jet-engines, Vol. 25, No. 3*, Vol. 17, No. 3, 2000, pp. 227–240. doi:10.1515/TJJ.2000.17.3.227

[21] So, R. M. C., Zhang, H. S., and Speziale, C. G., "Near-Wall Modeling of the Dissipation-Rate Equation," AIAA Paper 1992-0441, Jan. 1992.

[22] Lesieur, M., Métais, O., and Comte, P., "Introduction to LES," *Large-Eddy Simulations of Turbulence*, Cambridge Univ. Press, New York, 2005, pp. 12–20.

[23] Aupoix, B., "Modelling of Compressibility Effects in Mixing Layers," *Journal of Turbulence* [online journal], Vol. 5, No. N7, Feb. 2004. doi: 10.1088/1468-5248/5/1/007

[24] Boris, J., Grinstein, F., Orana, E., and Kolbea, R., "New Insights into Large Eddy Simulation," *Fluid Dynamics Research*, Vol. 10, 1992, pp. 199–228. doi:10.1016/0169-5983(92)90023-P

[25] Liou, M., and Steffen, C. J., "A New Flux Splitting Scheme," *Journal of Computational Physics*, Vol. 107, No. 1, 1993, pp. 23–39. doi:10.1006/jcph.1993.1122

[26] Meinke, M., Schröder, W., Krause, E., and Rister, T., "A Comparison of Second and Sixth-Order Methods for Large-Eddy Simulations," *Computers and Fluids*, Vol. 31, No. 4–7, 2002, pp. 695–718. doi:10.1016/S0045-7930(01)00073-1

[27] Alkishriwi, N., Meinke, M., and Schröder, W., "A Large-Eddy Simulation Method for Low Mach Number Flows Using Preconditioning and Multigrid," *Computers and Fluids*, Vol. 35, No. 10, 2006, pp. 1126–1136. doi:10.1016/j.compfluid.2005.06.002

[28] Renze, P., Schröder, W., and Meinke, M., "Large-Eddy Simulation of Film Cooling Flows at Density Gradients," *International Journal of Heat and Fluid Flow*, Vol. 29, No. 1, 2008, pp. 18–34. doi:10.1016/j.ijheatfluidflow.2007.07.010

[29] Guo, X., Schröder, W., and Meinke, M., "Large-Eddy Simulations of Film Cooling Flows," *Computers and Fluids*, Vol. 35, No. 6, 2006, pp. 587–606. doi:10.1016/j.compfluid.2005.02.007

[30] El-Askary, W. A., Schröder, W., and Meinke, M., "LES of Compressible Wall-Bounded Flows," 16th AIAA Computational Fluid Dynamics Conference, Orlando, FL, AIAA Paper 2003-3554, June 2003.

[31] Lund, T. S., and Xiaohua, W., and Squires, K. D., "Generation of Turbulent Inflow Data for Spatially-Developing Boundary Layer Simulations," *Journal of Computational Physics*, Vol. 140, No. 2, 1998, pp. 233–258. doi:10.1006/jcph.1998.5882

[32] Urbin, G., and Knight, D., "Large-Eddy Simulation of a Supersonic Boundary Layer Using an Unstructured Grid," *AIAA Journal*, Vol. 39, No. 7, 2001, pp. 1288–1295. doi:10.2514/2.1471

[33] Guarini, S. E., Moser, R. D., Shariff, K., and Wray, A., "Direct Numerical Simulation of a Supersonic Turbulent Boundary Layer at Mach 2.5," *Journal of Fluid Mechanics*, Vol. 414, 2000, pp. 1–33. doi:10.1017/S0022112000008466

[34] Jeong, J., and Hussain, F., "On the Identification of a Vortex," *Journal of Fluid Mechanics*, Vol. 285, 1995, pp. 69–94.
doi:10.1017/S0022112095000462

[35] Kanda, T., Masuya, G., Ono, F., and Wakamatsu, Y., "Effect of Film Cooling/Regenerative Cooling on Scramjet Engine Performance," *Journal of Propulsion and Power*, Vol. 10, No. 5, 1994, pp. 618–624.
doi:10.2514/3.23771

[36] König, D., Schröder, W., and Meinke, M., "Embedded LES-to-RANS Boundary in Zonal Simulations," *Journal of Turbulence*, Vol. 11, 2010, p. N7.
doi: 10.1080/14685241003698159

[37] Nagano, Y., Pei, C., and Hattori, H., "A New Low-Reynolds-Number One-Equation Model of Turbulence," *Flow, Turbulence and Combustion*, Vol. 63, 2000, pp. 135–151.
doi:10.1023/A:1009924002401

[38] Ahlman, D., Velter, G., Brethouwer, G., and Johansson, A. V., "Direct Numerical Simulation of Nonisothermal Turbulent Wall Jets," *Physics of Fluids*, Vol. 21, No. 3, 2009, pp. 035101.
doi:10.1063/1.3081554

[39] Pirozzoli, S., and Grasso, F., "Direct Numerical Simulation of Impinging Shock Wave/Turbulent Boundary Layer Interaction at $M = 2.25$," Vol. 18, No. 6, 2006, pp. 065113.
doi: 10.1063/1.2732460

[40] Juhany, K., "*Supersonic Film Cooling Including the Effect of Shock Wave Interaction*," Ph.D. Thesis, California Inst. of Technology, Pasadena, CA, 1994.

P. Tucker
Associate Editor